UNIVERSITY OF AMSTERDAM

UvA-DARE (Digital Academic Repository)

Relative measurement and extrapolation of the scintillation quenching factor of α -particles in liquid argon using DEAP-3600 data

DEAP Collaboration; Adhikari, P.; Pollmann, T.R.

DOI
10.1140/epjc/s10052-024-13518-7

Publication date
2025

Document Version
Final published version

Published in
European Physical Journal C

License
CC BY

Link to publication

Citation for published version (APA):
DEAP Collaboration, Adhikari, P., & Pollmann, T. R. (2025). Relative measurement and extrapolation of the scintillation quenching factor of α -particles in liquid argon using DEAP-3600 data. *European Physical Journal C*, *85*(1), Article 87. https://doi.org/10.1140/epjc/s10052-024-13518-7

General rights
It is not permitted to download or to forward/distribute the text or part of it without the consent of the author(s) and/or copyright holder(s), other than for strictly personal, individual use, unless the work is under an open content license (like Creative Commons).

Disclaimer/Complaints regulations
If you believe that digital publication of certain material infringes any of your rights or (privacy) interests, please let the Library know, stating your reasons. In case of a legitimate complaint, the Library will make the material inaccessible and/or remove it from the website. Please Ask the Library: https://uba.uva.nl/en/contact, or a letter to: Library of the University of Amsterdam, Secretariat, P.O. Box 19185, 1000 GD Amsterdam, The Netherlands. You will be contacted as soon as possible.

UvA-DARE is a service provided by the library of the University of Amsterdam (https://dare.uva.nl)

Download date:14 Oct 2026

Eur. Phys. J. C (2025) 85:87
https://doi.org/10.1140/epjc/s10052-024-13518-7

THE EUROPEAN PHYSICAL JOURNAL C

Regular Article - Experimental Physics

Relative measurement and extrapolation of the scintillation quenching factor of α-particles in liquid argon using DEAP-3600 data

DEAP Collaboration[⋆]

P. Adhikari[6], M. Alpízar-Venegas[15], P.-A. Amaudruz[26], J. Anstey[6,28], D. J. Auty[1], M. Batygov[13], B. Beltran[1], C. E. Bina[1,28], W. Bonivento[10], M. G. Boulay[6], J. F. Bueno[1], B. Cai[6,28], M. Cárdenas-Montes[7], S. Choudhary[2], B. T. Cleveland[24,13], R. Crampton[6,28], S. Daugherty[24,13,6], P. DelGobbo[6,28], P. Di Stefano[21], G. Dolganov[17], L. Doria[20], F. A. Duncan[24,a] and M. Dunford[6,28], E. Ellingwood[21], A. Erlandson[6,4], S. S. Farahani[1], N. Fatemighomi[24,22], G. Fiorillo[8,12], R. J. Ford[24,13], D. Gahan[3,10], D. Gallacher[6], P. García Abia[7], S. Garg[6], P. Giampa[21,26], A. Giménez-Alcázar[7], D. Goeldi[6,28], P. Gorel[24,13], K. Graham[6], A. L. Hallin[1], M. Hamstra[6,21], S. Haskins[6,28], J. Hu[1], J. Hucker[21], T. Hugues[2,21], A. Ilyasov[17,18], B. Jigmeddorj[24,13], C. J. Jillings[24,13], G. Kaur[6], M. Khoshraftar Yazdi[1], A. Kemp[22,21], M. Kuźniak[2,6,28], F. La Zia[22], M. Lai[5], S. Langrock[13,28], B. Lehnert[14], N. Levashko[17], M. Lissia[10], L. Luzzi[7], I. Machulin[17,18], A. Maru[6,28], J. Mason[6,28], A. B. McDonald[21], T. McElroy[1], J. B. McLaughlin[22,26], C. Mielnichuk[1], L. Mirasola[3,10], A. Moharana[6], J. Monroe[22], A. Murray[21], C. Ng[1], G. Oliviéro[6,28], M. Olszewski[2], S. Pal[1,28], D. Papi[1], B. Park[1], M. Perry[6], V. Pesudo[7], T. R. Pollmann[13,21,27,29], F. Rad[6,28], C. Rethmeier[6], F. Retière[26], L. Roszkowski[2,16], R. Santorelli[7], F. G. Schuckman II[21], S. Seth[6,28], V. Shalamova[5], P. Skensved[21], T. Smirnova[17], K. Sobotkiewich[6], T. Sonley[24,6,28], J. Sosiak[6,28], J. Soukup[1], R. Stainforth[6], M. Stringer[21,28], J. Tang[1], E. Vázquez-Jáuregui[15], S. Viel[6,28], B. Vyas[6], M. Walczak[2], J. Walding[22], M. Ward[21], S. Westerdale[5], R. Wormington[21]

[1] Department of Physics, University of Alberta, Edmonton, AB T6G 2R3, Canada
[2] AstroCeNT, Nicolaus Copernicus Astronomical Center, Polish Academy of Sciences, Rektorska 4, 00-614 Warsaw, Poland
[3] Physics Department, Università degli Studi di Cagliari, 09042 Cagliari, Italy
[4] Canadian Nuclear Laboratories, Chalk River, ON K0J 1J0, Canada
[5] Department of Physics and Astronomy, University of California, Riverside, CA 92521, USA
[6] Department of Physics, Carleton University, Ottawa, ON K1S 5B6, Canada
[7] Centro de Investigaciones Energéticas, Medioambientales y Tecnológicas, Madrid 28040, Spain
[8] Physics Department, Università degli Studi "Federico II" di Napoli, Naples 80126, Italy
[9] Astronomical Observatory of Capodimonte, Salita Moiariello 16, I-80131 Naples, Italy
[10] INFN Cagliari, 09042 Cagliari, Italy
[11] INFN Laboratori Nazionali del Gran Sasso, Assergi, (AQ) 67100, Italy
[12] INFN Napoli, Naples 80126, Italy
[13] School of Natural Sciences, Laurentian University, Sudbury, ON P3E 2C6, Canada
[14] Nuclear Science Division, Lawrence Berkeley National Laboratory, Berkeley, CA 94720, USA
[15] Instituto de Física, Universidad Nacional Autónoma de México, A. P. 20-364, Ciudad de México 01000, Mexico
[16] BP2, National Centre for Nuclear Research, ul. Pasteura 7, 02-093 Warsaw, Poland
[17] National Research Centre Kurchatov Institute, Moscow 123182, Russia
[18] National Research Nuclear University MEPhI, Moscow 115409, Russia
[19] Physics Department, Princeton University, Princeton, NJ 08544, USA
[20] PRISMA+ Cluster of Excellence and Institut für Kernphysik, Johannes Gutenberg-Universität Mainz, 55128 Mainz, Germany
[21] Department of Physics, Engineering Physics and Astronomy, Queen's University, Kingston, ON K7L 3N6, Canada
[22] Royal Holloway University London, Egham Hill, Egham, Surrey TW20 0EX, UK
[23] Rutherford Appleton Laboratory, Harwell Oxford, Didcot OX11 0QX, UK
[24] SNOLAB, Lively, ON P3Y 1M3, Canada

Published online: 27 January 2025

[25] University of Sussex, Sussex House, Brighton, East Sussex BN1 9RH, UK
[26] TRIUMF, Vancouver, BC V6T 2A3, Canada
[27] Department of Physics, Technische Universität München, 80333 Munich, Germany
[28] Arthur B. McDonald Canadian Astroparticle Physics Research Institute, Queen's University, Kingston, ON K7L 3N6, Canada
[29] Currently at Nikhef and the University of Amsterdam, Science Park, 1098 XG Amsterdam, Netherlands
a Deceased

Received: 12 June 2024 / Accepted: 21 October 2024
© The Author(s) 2025

Abstract The knowledge of scintillation quenching of α-particles plays a paramount role in understanding α-induced backgrounds and improving the sensitivity of liquid argon-based direct detection of dark matter experiments. We performed a relative measurement of scintillation quenching in the MeV energy region using radioactive isotopes (^{222}Rn, ^{218}Po and ^{214}Po isotopes) present in trace amounts in the DEAP-3600 detector and quantified the uncertainty of extrapolating the quenching factor to the low-energy region.

1 Introduction

Over the past decade, liquid argon (LAr) detectors have been extensively used for dark matter direct detection experiments due to the high purity, scalability and excellent scintillation efficiency of this material [1–5]. These experiments are optimized to primarily measure the scintillation signals induced by low-energy nuclear recoils that could be produced due to elastic scattering of weakly interacting massive particles (WIMPs), a promising dark matter candidate. Because the WIMP interaction rate is extremely low, mitigating background events is an inevitable requirement of such a detection procedure.

The scintillation time profiles of LAr due to electronic recoils (ERs) and nuclear recoils (NRs) differ from each other [6,7]. This characteristic helps to reduce ER backgrounds due to ^{39}Ar β decays using the pulse-shape discrimination (PSD) technique [8]. DEAP-3600 achieved the most sensitive limit on the spin-independent WIMP-nucleon cross-section on argon above 30 GeV/c^2 WIMP mass [1]. The sensitivity of the DEAP-3600 experiment is limited by the presence of intrinsic α-backgrounds. The most challenging such backgrounds come from α-decays within the trace amount of dust particulates dispersed in the LAr volume, and from α-decays of ^{210}Po on the flowguides in the neck of the detector, following which the scintillation light is shadowed.

In order to correctly model α-induced backgrounds, the amount of scintillation light induced by α-particles in LAr must be understood over a wide range of energy. This can be quantified by considering the fraction of deposited energy that is dissipated as scintillation photons: this ratio is known as the quenching factor (QF). A number of experimental studies have been performed to measure the scintillation yield due to neutron-induced NRs in LAr in the low-energy region [9–12]. The scintillation quenching at low energies cannot completely be explained by the Lindhard et al. theory [13] and various models have been proposed to understand the light yield for low-energy NRs in LAr [11,12,14,15]. In contrast to NRs, few measurements are available for studying scintillation light due to α-particles in LAr at high energies using a ^{210}Po source [16–18]. In the absence of a universally accepted α-quenching model, we explore the scintillation yield of α-particles over a wide energy region (tens of keV to a few MeV) and quantify extrapolation uncertainties.

The main objective of the present work is to generate an energy-dependent scintillation quenching curve for α-particles in LAr and probe the uncertainty of extrapolating the α-particle QF to the low-energy region for LAr. As input to the extrapolation procedure, we start from the direct measurement of the scintillation QF of α-particles from ^{210}Po reported in Ref. [16], and perform a relative measurement of the QF using full-energy α peaks from the ^{222}Rn chain using DEAP-3600 data. Using such a relative measurement reduces the impact of systematic uncertainties related to the detector response and absolute energy calibration. Based on the results in the MeV range, a model is then used to extrapolate the α-particle QF into the low-energy region for LAr.

Section 2 presents a brief description of the DEAP-3600 detector as well as data selection. The relative measurement of the scintillation QF for α-particles in the MeV energy region is described in Sect. 3. In Sect. 4, we extrapolate the energy-dependent α-particle QF and estimate the uncertainties down to energy values in the tens of keV range. Finally, we summarize the results in Sect. 5.

2 Detector and data selection

The DEAP-3600 detector contains 3.3 tonnes of LAr within a spherical acrylic vessel (AV) of radius 850 mm. The top 300 mm of the spherical detector region contains gaseous argon (GAr). A detailed description of the detector is given

*e-mail: deap-papers@snolab.ca

Table 1 The short-lived α-decays of interest in LAr [19–22]. The activity of these isotopes in the DEAP-3600 detector was estimated in Ref. [1]

Radioactive isotope	Half-life	Branching ratio (%)	α-particle energy (MeV)	Q-value (MeV)	Activity in DEAP-3600 (μBq/kg of LAr)
^{222}Rn	3.8 days	99.92	5.489	5.590	0.153 ± 0.005
^{218}Po	3.1 min	99.9989	6.002	6.115	0.159 ± 0.005
^{214}Po	164.3 μs	99.9895	7.686	7.833	0.153 ± 0.005

in Ref. [23]. The inner surface of the AV is coated with a 3 μm layer of 1,1,4,4-tetraphenyl-1,3-butadiene (TPB) wavelength shifter which converts 128 nm scintillation light produced by LAr to visible light that peaks at 420 nm. The light signal is acquired by 255 inward-facing Hamamatsu R5912-HQE photomultiplier tubes (PMTs) which have high quantum efficiency and low radioactivity [24]. The PMT signals are digitized by both high-gain (CAEN V1720) and low-gain (CAEN V1740) waveform digitizer channels. Signals from the high-gain digitizer channels are used in this analysis.

Data are processed using the RAT [25] software framework adapted for DEAP-3600 data. The charge of a pulse detected in a PMT is divided by the average single-PE charge of the PMT, known from calibrations, to obtain the number of recorded photoelectrons (PEs). This analysis uses the full dataset collected by DEAP-3600 from November 2016 to December 2017, plus 20% of the dataset collected from January 2018 to March 2020. This corresponds to 388.4 live-days.

Events are observed due to α-decays from the ^{222}Rn isotope and its descendants, occurring inside the detector including the LAr target [1]. Starting from ^{222}Rn, three α-particles and two β-particles are emitted following the sequence of transitions before producing the long-lived isotope ^{210}Pb, the chain with the highest probability being:

$$^{222}_{86}\mathrm{Rn} \xrightarrow{\alpha} {}^{218}_{84}\mathrm{Po} \xrightarrow{\alpha} {}^{214}_{82}\mathrm{Pb} \xrightarrow{\beta} {}^{214}_{83}\mathrm{Bi} \xrightarrow{\beta} {}^{214}_{84}\mathrm{Po} \xrightarrow{\alpha} {}^{210}_{82}\mathrm{Pb}.$$

In this work, we consider α-particles emitted from short-lived decays and depositing their full energy in the LAr volume. These α-emitting isotopes are detailed in Table 1. From the long-lived ^{210}Pb isotope (22.2 year half-life), the ^{210}Po isotope is produced following two β-decays:

$$^{210}_{82}\mathrm{Pb} \xrightarrow{\beta} {}^{210}_{83}\mathrm{Bi} \xrightarrow{\beta} {}^{210}_{84}\mathrm{Po} \quad .$$

We do not consider α-decays from ^{210}Po in the relative QF measurement, because in DEAP-3600 these decays mostly originate from the inner surface of the AV: the resulting α-particles deposit an unknown portion of their energy into the acrylic and TPB before creating scintillation signals in LAr [1].

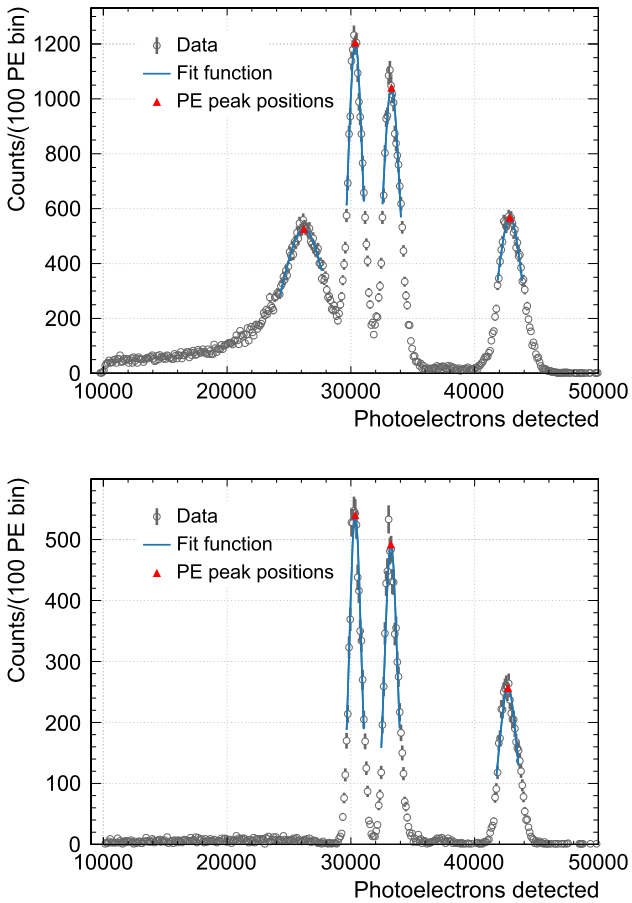

Fig. 1 Distribution of the number of PE detected from α-decay events the position of which is reconstructed within radius 0–850 mm (top histogram) and 0–600 mm (bottom histogram) from the origin of the detector. From left to right, the peaks are from the decay of the ^{210}Po, ^{222}Rn, ^{218}Po and ^{214}Po isotopes. Each peak is fitted by a Gaussian distribution (blue line). Red solid points are the detected peak PE positions from each Gaussian fit

Event selection cuts are applied to the data in order to select α-decay candidates. First, the same run selection, trigger requirements and data cleaning cuts as in Ref. [1] are applied. Then, to remove pre-trigger pileup and post-trigger pileup from coincidence events, the event trigger time must be within the range [2250, 2700] ns in the trigger window, be recorded at least 20 μs after the previous event's trigger time, and with fewer than 4 pulses recorded by PMTs in the

first 1600 ns of the event. Events are rejected if more than 75% of the PE in the event were detected by a single PMT. To select events from the NR band and reject ERs, a PSD cut is applied with the requirement that at least 55% of the PE are detected within $[-28, 150]$ ns of the trigger time. Finally, the reconstructed position of the event must be within the LAr volume.

Figure 1 shows the PE distribution of the selected events at high PE, with α peaks observed from the decay of ^{210}Po, ^{222}Rn, ^{218}Po and ^{214}Po isotopes. Each peak is fitted by a Gaussian distribution using TMinuit [26] in ROOT [27] and the mean of the each fit function is considered as the PE peak value.

3 Relative measurement of the quenching factor

3.1 Method

The scintillation quenching, QF_α, of α-particles with energy E_α can be expressed by the following equation:

$$\mathrm{QF}_\alpha = \frac{\mathrm{PE}_\alpha}{Y \times E_{\alpha,\mathrm{dep}}} \quad , \tag{1}$$

where PE_α is the detected number of PE at the peak, $E_{\alpha,\mathrm{dep}}$ is the total energy deposited by the α-particles within LAr, and Y (in PE/keV) is the scintillation light yield measured for γ-rays, which is assumed to be linear over the 5–8 MeV range. For the α-decays observed on-peak, the full energy is deposited within the LAr volume of the detector, therefore we take $E_{\alpha,\mathrm{dep}} = E_\alpha$ from Table 1. We assume that the number of detected PE generated by the heavy nuclear recoils in these events is negligible compared to the amount generated by the full-energy α-particles.

The DEAP-3600 detector is calibrated at low energy from around 565 keV to 1.3 MeV using β-decays from naturally present ^{39}Ar isotopes in LAr and an external ^{22}Na γ source. The energy response function is linear over a wide range of energies, whereas a non-linear response has been observed above a few MeV because of the saturation of detected pulses. Saturation of the PMTs and digitizers can occur; digitizer clipping effects start at lower PE compared to the region where PMT non-linearity effects are observed. In energy reconstruction, a correction algorithm is used to deal with such effects. As a first step, this algorithm identifies clipped pulses. For each such pulse, the charge measured in high-gain digitizer channels is corrected using a function that was obtained by comparing the pulse integrals of a large number of unsaturated pulses recorded by high-gain digitizer channels to the corresponding pulses recorded by low-gain digitizer channels. This reconstructed charge is used to recalculate the number of PE, after which another correction is applied to account for the non-linear PMT response which appears due to space-charge effects within the PMT dynode structure. For this purpose, a sigmoidal function is used to model charge growth in a PMT in the presence of space-charge. This function controls both the PE value at which saturation begins and the nature of the gradual change in the saturation effect through three parameters determined by tuning with data. Pulses from events originating close to the AV surface are more likely to be saturated. The magnitude of the entire correction procedure is typically less than 1%; it can range up to 10% for most pulses, and rarely up to 50% for pulses from high-energy events closest to the AV surface. This has an indirect dependence on the reconstructed position of the events, systematic uncertainties from which are taken into account in the next section. A detailed description of this procedure is provided in Ref. [28].

This analysis uses three data points: the measurement of $\mathrm{QF}_{\alpha,^{210}\mathrm{Po}} = 0.710 \pm 0.028$ at 5.305 MeV by Doke et al. [16]; and the following two relative measurements from DEAP-3600. Based on Eq. 1, we define the ratios R_2 and R_3 as follows:

$$\frac{\mathrm{QF}_{\alpha,^{218}\mathrm{Po}}}{\mathrm{QF}_{\alpha,^{222}\mathrm{Rn}}} = \frac{\mathrm{PE}_{\alpha,^{218}\mathrm{Po}}}{\mathrm{PE}_{\alpha,^{222}\mathrm{Rn}}} \times \frac{E_{\alpha,^{222}\mathrm{Rn}}}{E_{\alpha,^{218}\mathrm{Po}}} \equiv R_2 \times \frac{E_{\alpha,1}}{E_{\alpha,2}}, \tag{2}$$

$$\frac{\mathrm{QF}_{\alpha,^{214}\mathrm{Po}}}{\mathrm{QF}_{\alpha,^{222}\mathrm{Rn}}} = \frac{\mathrm{PE}_{\alpha,^{214}\mathrm{Po}}}{\mathrm{PE}_{\alpha,^{222}\mathrm{Rn}}} \times \frac{E_{\alpha,^{222}\mathrm{Rn}}}{E_{\alpha,^{214}\mathrm{Po}}} \equiv R_3 \times \frac{E_{\alpha,1}}{E_{\alpha,3}}. \tag{3}$$

where on the right, the subscripts 1, 2, 3 are used for ^{222}Rn, ^{218}Po and ^{214}Po respectively.

By taking the ratios of the peak PE values for α-particles within the 5 to 8 MeV range, the effect of non-linearities in the light detection efficiency on the estimation of the QF is reduced, and the analysis becomes less sensitive to the absolute energy calibration at high energy. These ratios for ^{218}Po and ^{214}Po relative to ^{222}Rn are calculated using Gaussian fits to the whole dataset as shown in Fig. 1 (top): the resulting measured values of R_2 and R_3 are given in Table 2.

3.2 Systematic uncertainties

The light yield Y depends on various detector parameters, such as the photo-detection efficiency of the PMTs, the reflectivity of the AV surface, the roughness of the AV inner surface, the efficiency and thickness of TPB, etc. Some of these properties could vary throughout the data taking period or different locations within the detector. Therefore, the uncertainties on R_2 and R_3 are estimated in terms of their observed variations as a function of reconstructed position and time of occurrence of the α-decays within the LAr throughout the data-taking period.

To estimate uncertainties due to α-decay position (σ_p), the detector volume is divided into four concentric spheri-

Table 2 Quenching factor of α-particles obtained from the relative measurement using ^{222}Rn, ^{218}Po and ^{214}Po decays within the DEAP-3600 detector. The measured value by Ref. [16] of the QF for α-particles from ^{210}Po decays is also shown

Radioactive isotope	Energy of α-particle (MeV)	Ratio of PE peak to ^{222}Rn PE peak (R_i)	Uncertainty on the peak PE ratio (σ_i)	Quenching factor (QF_α)	Uncertainty on QF_α due to PE peak ratios	Absolute uncertainty on QF_α
^{210}Po	5.305	–	–	0.710 [16]	–	0.028 [16]
^{218}Po	6.002	1.096	0.002	0.712	0.001	–
^{214}Po	7.686	1.411	0.006	0.716	0.003	–

cal regions where the distance to the origin of the detector is 0–200 mm, 200–400 mm, 400–600 mm and 600–800 mm. The LAr volume which is within 50 mm from the inner surface of the AV is not considered here because the PE peak from the α-decay of ^{210}Po on the AV surface is the dominant contribution there. For each region, the peak PE values from ^{222}Rn, ^{218}Po and ^{214}Po are each determined as the mean of the corresponding Gaussian fit. Averaged over all four regions, the ratios of ^{218}Po and ^{214}Po peak PE to the ^{222}Rn peak PE are respectively 1.096 ± 0.001 and 1.408 ± 0.005.

In order to estimate the uncertainties due to time of occurrence of α-decays in the detector (σ_t), the entire dataset is divided into twenty-one time bins, each covering sixty days except the last bin. The peak PE ratios are estimated for each time bin. Unlike the previous case, events originating near the inner surface of the detector are also considered here. Averaged over time bins, the peak PE ratios relative to ^{222}Rn are 1.096 ± 0.002 for ^{218}Po and 1.412 ± 0.003 for ^{214}Po.

Assuming the systematic uncertainties from event position and time are uncorrelated, their sum in quadrature is taken as the absolute uncertainty $\sigma_i = \sqrt{(\sigma_{p,i})^2 + (\sigma_{t,i})^2}$ on the peak PE ratio R_i, overall resulting in $R_2 = 1.096 \pm 0.002$ and $R_3 = 1.411 \pm 0.006$.

If we further assume that at 5.489 MeV, $\mathrm{QF}_{\alpha,^{222}\mathrm{Rn}} = \mathrm{QF}_{\alpha,^{210}\mathrm{Po}}$ measured in Ref. [16], it follows from rearranging Eqs. 2 and 3 that $\mathrm{QF}_{\alpha,^{218}\mathrm{Po}} = 0.712 \pm 0.001$ and $\mathrm{QF}_{\alpha,^{214}\mathrm{Po}} = 0.716 \pm 0.003$ with the uncertainties due to relative PE peak positions only. The total uncertainty on these QF values is dominated by the absolute uncertainty of ± 0.028 from the measurement of $\mathrm{QF}_{\alpha,^{210}\mathrm{Po}}$.

4 Extrapolation of the quenching factor

With the help of the existing experimental data [29–32], Mei et al. [14] proposed a prescription which predicts that the scintillation quenching of neutron-induced nuclear recoils in noble liquids from a few tens of keV to a few hundreds of keV is influenced by two different mechanisms: reduction of energy transferred to electrons, and consequently production of a smaller number of excimers and ions; and reduction of scintillation yield due to high ionization and excitation density.

Here, we use a model that considers two independent quenching effects: a "nuclear QF" accounting for the fraction of energy lost by a recoiling nucleus as a result of nuclear collisions, and an "electronic QF" accounting for non-radiative de-excitation of excimers produced by energy transferred to atomic electrons. The product of these two factors will be taken as the final result.

4.1 Nuclear quenching factor

The ratio of energy transferred to electrons ($E_{\mathrm{dep,elec}}$) to the total energy deposition, where this denominator includes the part responsible for nuclear translation motion ($E_{\mathrm{dep,nucl}}$) along the α-particle's track, is defined as the nuclear QF:

$$\mathrm{QF}_\alpha^{\mathrm{nucl}} = \frac{E_{\mathrm{dep,elec}}}{E_{\mathrm{dep,elec}} + E_{\mathrm{dep,nucl}}} \quad , \tag{4}$$

and the uncertainty on this calculation is taken as

$$\begin{aligned}
\Delta\mathrm{QF}_\alpha^{\mathrm{nucl}} &= \left[\left(\frac{\partial \mathrm{QF}_\alpha^{\mathrm{nucl}}}{\partial E_{\mathrm{dep,elec}}} \sigma_{\mathrm{elec}} \right)^2 + \left(\frac{\partial \mathrm{QF}_\alpha^{\mathrm{nucl}}}{\partial E_{\mathrm{dep,nucl}}} \sigma_{\mathrm{nucl}} \right)^2 \right. \\
&\quad \left. + 2\rho\sigma_{\mathrm{elec}}\sigma_{\mathrm{nucl}} \left(\frac{\partial \mathrm{QF}_\alpha^{\mathrm{nucl}}}{\partial E_{\mathrm{dep,elec}}} \right) \left(\frac{\partial \mathrm{QF}_\alpha^{\mathrm{nucl}}}{\partial E_{\mathrm{dep,nucl}}} \right) \right]^{1/2} \\
&= \left[\left(\frac{E_{\mathrm{dep,nucl}} \cdot \sigma_{\mathrm{elec}}}{\left(E_{\mathrm{dep,elec}} + E_{\mathrm{dep,nucl}}\right)^2} \right)^2 \right. \\
&\quad + \left(\frac{-E_{\mathrm{dep,elec}} \cdot \sigma_{\mathrm{nucl}}}{\left(E_{\mathrm{dep,elec}} + E_{\mathrm{dep,nucl}}\right)^2} \right)^2 \qquad (5) \\
&\quad \left. - 2\rho \cdot \frac{E_{\mathrm{dep,nucl}} \cdot E_{\mathrm{dep,elec}} \cdot \sigma_{\mathrm{elec}} \cdot \sigma_{\mathrm{nucl}}}{\left(E_{\mathrm{dep,elec}} + E_{\mathrm{dep,nucl}}\right)^4} \right]^{1/2} \qquad (6) \\
&= \sqrt{2(1-\rho)} \frac{E_{\mathrm{dep,elec}}\ E_{\mathrm{dep,nucl}}}{(E_{\mathrm{dep,elec}} + E_{\mathrm{dep,nucl}})^2} \sigma_{\mathrm{rel}} \qquad (7)
\end{aligned}$$

where $\rho = -1$ is the correlation coefficient between $E_{\mathrm{dep,elec}}$ and $E_{\mathrm{dep,nucl}}$ which are anti-correlated for a fixed total energy

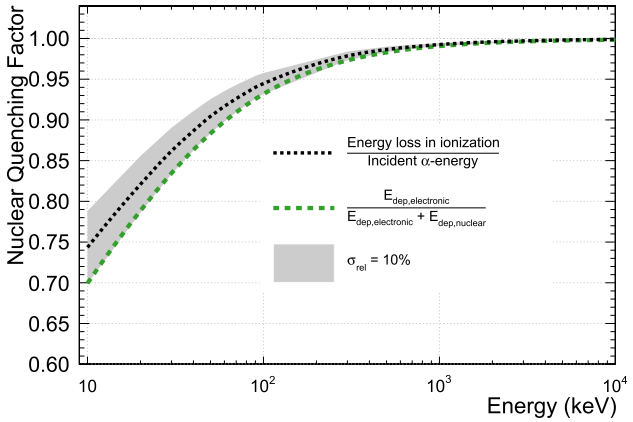

Fig. 2 Nuclear QF curve for α-particles estimated using SRIM stopping power tables and Eq. 4 (green) and TRIM simulation (black)

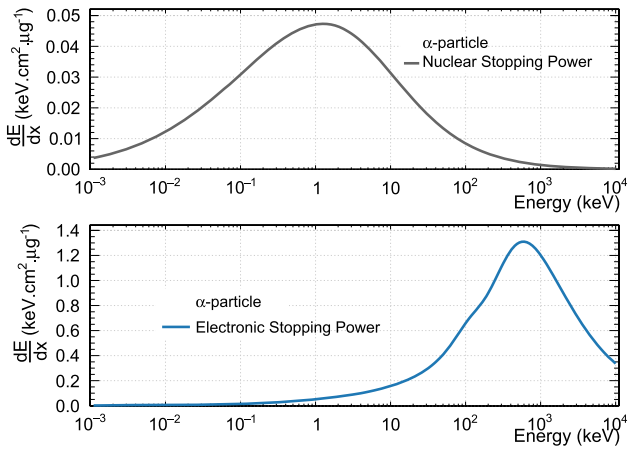

Fig. 3 Stopping power curves for α-particles in LAr from SRIM-2013 [34]

deposition. In the last step it is assumed that the relative uncertainties are similar: $\frac{\sigma_{\text{elec}}}{E_{\text{dep,elec}}} = \frac{\sigma_{\text{nucl}}}{E_{\text{dep,nucl}}} = \sigma_{\text{rel}}$.

To calculate this nuclear QF as a function of energy, TRIM (TRansport of Ions in Matter) simulations [33] are performed for α-particle energies between 10 keV and 10 MeV. This simulation provides the energy loss in ionization, phonon generation and radiation damage. The option named "Ion Distribution and Quick Calculation of Damage" is used to minimize the detailed estimation of target damage. To calculate the nuclear QF, the energy loss from ionization estimated using TRIM simulations is divided by the incident energy of the α-particle. The results are shown in Fig. 2.

Also shown in Fig. 2 is the result of a cross-check calculation of the nuclear QF where the electronic and nuclear stopping power values are taken from SRIM (The Stopping and Range of Ions in Matter)-2013 [34] as shown in Fig. 3. The deposited energy is calculated in steps of 1 nm along the path of the α-particle track. SRIM calculates the separate electronic and nuclear stopping powers of the α-particle; this accounts for the amount of energy transferred to atomic electrons and nuclei directly, but does not account for the subsequent scatters and the final state distribution of the energy deposited. The resulting nuclear QF curve for α-particles in LAr is calculated using Eq. 4.

In the present study, the values of the nuclear QF obtained using TRIM simulations are used in the combined QF calculation of Sect. 4.3. The nuclear QF values from TRIM are about 2–6% higher than the values obtained using the SRIM stopping power in the range 10–60 keV. This difference decreases with increasing α energy and becomes less than 1% from around 300 keV. The stopping power calculation from SRIM deviates from the experimental data points by a maximum of approximately 10% for helium ions within an argon gas target [33]. Therefore, the relative uncertainty σ_{rel} is considered as 10% here. The nuclear QF uncertainty is calculated using Eq. 7 and shown in gray colored band in Fig. 2.

4.2 Electronic quenching factor

Next, using Birks's formalism [35], we account for the non-radiative de-excitation of excimers by interactions with atomic electrons. For the fraction of the energy deposited in a small step that is converted to scintillation light, we write:

$$\frac{dy}{dE} = \frac{A}{1 + B\frac{dE}{dx}}, \tag{8}$$

where $\frac{dE}{dx}$ is the electronic stopping power at each step along the α-particle's track, and A and B are constants for any α-particle energy. In this model, A accounts for average quenching due to the density of the deposition within the track core, and B accounts for the change in density with energy.

The total energy that goes into scintillation along the α-particle track is then:

$$y(E_\alpha) = A\int_0^{E_\alpha} \frac{dE}{1 + B\frac{dE}{dx}}. \tag{9}$$

We define the electronic quenching factor from this model as the fraction of energy that goes into scintillation:

$$\text{QF}_\alpha^M = \frac{y(E_\alpha)}{E_\alpha} = \frac{A}{E_\alpha}\int_0^{E_\alpha} \frac{dE}{1 + B\frac{dE}{dx}}. \tag{10}$$

The model predictions for the ratios R_i are likewise:

$$R_i^M = \frac{y(E_{\alpha,i})}{y(E_{\alpha,1})} = \frac{\int_0^{E_{\alpha,i}} \frac{dE}{1+B\frac{dE}{dx}}}{\int_0^{E_{\alpha,1}} \frac{dE}{1+B\frac{dE}{dx}}}. \tag{11}$$

We constrain the values of the parameters A and B using the measured values of $\text{QF}_{\alpha,^{210}\text{Po}}$ from Ref. [16] and the two

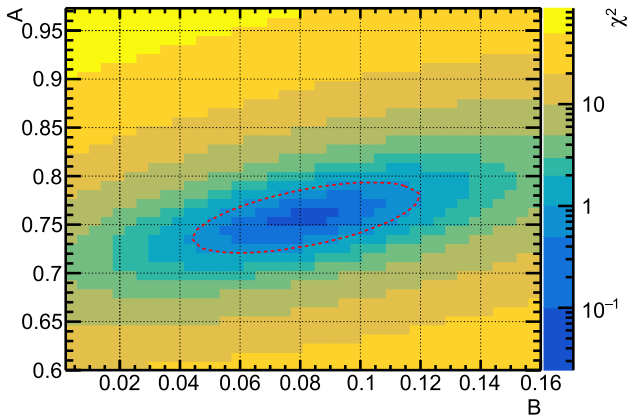

Fig. 4 χ^2 from Eq. 12 shown as a function of A and B. The red-dotted line represents the 1σ contour drawn in the (A, B) parameter space

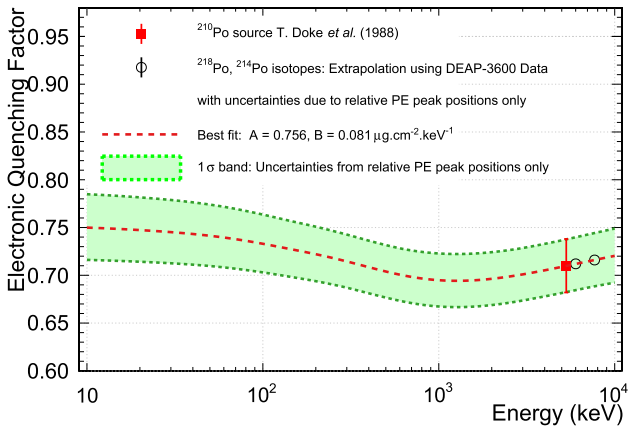

Fig. 5 Electronic QF as a function of α-particle energy. The best-fit QF curve is shown with the red dashed line. The green shaded region is the 1σ band considering only the uncertainties of the relative measurement, as a function of energy. This band encompasses the absolute uncertainty from the measurement of $\mathrm{QF}_{\alpha,^{210}\mathrm{Po}}$ which is the dominant uncertainty in this analysis. The red solid square represents T. Doke's measurement of the scintillation quenching of α-particles emitted from the decay of ^{210}Po [16]. Two black open circles display the DEAP-3600 relative measurements from ^{218}Po and ^{214}Po (see Table 2)

R_i from Sect. 3, by minimizing

$$\chi^2 = \frac{(\mathrm{QF}_{\alpha,^{210}\mathrm{Po}} - \mathrm{QF}^M_{\alpha,^{210}\mathrm{Po}})^2}{\sigma_0^2} + \sum_{i=2}^{3} \frac{\left(R_i - R_i^M\right)^2}{\sigma_i^2} \quad (12)$$

where as reported above the uncertainties are $\sigma_0 = 0.028$, $\sigma_2 = 0.002$ and $\sigma_3 = 0.006$. Using the electronic stopping power values from SRIM-2013 [34], this χ^2 is calculated in a grid of (A, B) values over the range $A = (0.600 - 1.000)$ and $B = (0.001 - 0.160)$: the result is shown in Fig. 4. The χ^2 is observed to be smooth, with a minimum at $A = 0.756$ and $B = 0.081\ \mu\mathrm{g} \cdot \mathrm{cm}^{-2} \cdot \mathrm{keV}^{-1}$. The resulting best-fit electronic QF curve is shown in Fig. 5.

Based on the χ^2 function, a 1σ contour is drawn in (A, B) parameter space where on the contour $\chi^2 = \chi^2_{\mathrm{min}} + 1$, with χ^2_{min} the minimum χ^2 value (corresponding to the best fit): this contour is also shown in Fig. 4. For different (A, B) combinations along this contour, the electronic QF is calculated as a function of α-particle energy using Eq. 10. The 1σ bands in Fig. 5 are generated by using the QF curves from the worst fits that are consistent with the data at the 1σ level.

4.3 Combined results

The final energy-dependent QF curve is obtained by taking the product of the best-fit electronic QF curve and the nuclear QF curve from TRIM. According to these results, at high energy the electronic quenching mechanism is dominant, while at low energy nuclear quenching becomes important.

Figure 6 displays the scintillation QF curve for α-particles in LAr and the corresponding $\pm 1\sigma$ uncertainty band over the energy range 10 keV–10 MeV, from the combination of the electronic QF with the nuclear QF. This uncertainty band comes from the combination of the 1σ band on the electronic

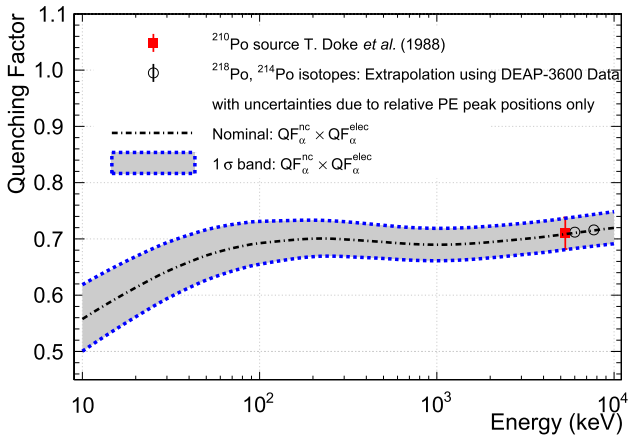

Fig. 6 Energy-dependent scintillation QF curve for α-particles within LAr, as a function of their energy on a logarithmic scale. The nominal and $\pm 1\sigma$ QF curves are the product of the electronic QF (see Fig. 5) with the nuclear QF from TRIM (see Fig. 2)

QF shown in Fig. 5 with the nuclear QF uncertainty calculated using Eq. 7 taking $\sigma_{\mathrm{rel}} = 10\%$.

Relative light yield measurements were performed by Hitachi et al. [17] within liquid argon by measuring the pulse heights of α-particles from ^{210}Po, ^{212}Bi, ^{252}Cf and ^{212}Po relative to 6 MeV α-particles. The resulting estimates of the quenching factors are consistent with our results within uncertainties.

5 Summary and outlook

In summary, α-particles from radioactive decays detected in LAr with the DEAP-3600 detector are used to perform a relative measurement of the QF at energies between 5.489 and 7.686 MeV, corresponding to the full-energy α peaks. One advantage of the relative measurement procedure is to reduce the impact of light-yield non-linearity effects observed in DEAP-3600 data above a few MeV. We extrapolated the QF values into the low-energy region down to 10 keV, and also assigned uncertainties to this extrapolation. The energy-dependent QF curve is utilized in the analysis of backgrounds to the WIMP search. Measurements of the QF at various energies are currently underway in order to validate these results.

Acknowledgements We thank SNOLAB and its staff for support through underground space, logistical, and technical services. SNOLAB operations are supported by the CFI and Province of Ontario MRI, with underground access provided by Vale at the Creighton mine site. We thank Vale for their continuing support, including the work of shipping the acrylic vessel underground. We gratefully acknowledge the support of the Digital Research Alliance of Canada, Calcul Québec, the Centre for Advanced Computing at Queen's University, and the Computational Centre for Particle and Astrophysics (C2PAP) at the Leibniz Supercomputer Centre (LRZ) for providing the computing resources required to undertake this work.

Funding We thank the Natural Sciences and Engineering Research Council of Canada (NSERC), the Canada Foundation for Innovation (CFI), the Ontario Ministry of Research and Innovation (MRI), and Alberta Advanced Education and Technology (ASRIP), the University of Alberta, Carleton University, Queen's University, the Canada First Research Excellence Fund through the Arthur B. McDonald Canadian Astroparticle Physics Research Institute, Consejo Nacional de Ciencia y Tecnología Project No. CONACYT CB-2017-2018/A1-S-8960, DGAPA UNAM Grants No. PAPIIT IN108020 and IN105923, and Fundación Marcos Moshinsky, the European Research Council Project (ERC StG 279980), the UK Science and Technology Facilities Council (STFC) (ST/K002570/1 and ST/R002908/1), the Leverhulme Trust (ECF-20130496), the Russian Science Foundation (Grant No. 21-72-10065), the Spanish Ministry of Science and Innovation (PID2019-109374GB-I00) and the Community of Madrid (2018-T2/TIC-10494), the International Research Agenda Programme AstroCeNT (MAB/2018/7) funded by the Foundation for Polish Science (FNP) from the European Regional Development Fund, and the Polish National Science Centre (2022/47/B/ST2/02015). Studentship support from the Rutherford Appleton Laboratory Particle Physics Division, STFC and SEPNet PhD is acknowledged.

Data Availability Statement Data will be made available on reasonable request. [Authors' comment: The data used in this paper requires approximately 150 TB of disk space and its interpretation requires an extensive understanding of the detector. Therefore, making the data publicly available is impractical. Access to the data may be granted on request to the DEAP collaboration (email: deap-papers@snolab.ca)].

Code Availability Statement Code/software will be made available on reasonable request. [Authors' comment: The software used in this paper is a large specialized set of codes for particular computing environments. Therefore, making the software publicly available is impractical. Access to the code may be granted on request to the DEAP collaboration.]

Open Access This article is licensed under a Creative Commons Attribution 4.0 International License, which permits use, sharing, adaptation, distribution and reproduction in any medium or format, as long as you give appropriate credit to the original author(s) and the source, provide a link to the Creative Commons licence, and indicate if changes were made. The images or other third party material in this article are included in the article's Creative Commons licence, unless indicated otherwise in a credit line to the material. If material is not included in the article's Creative Commons licence and your intended use is not permitted by statutory regulation or exceeds the permitted use, you will need to obtain permission directly from the copyright holder. To view a copy of this licence, visit http://creativecommons.org/licenses/by/4.0/.
Funded by SCOAP[3].

References

1. R. Ajaj et al., Phys. Rev. D **100**, 022004 (2019). https://doi.org/10.1103/PhysRevD.100.022004
2. P. Agnes et al., Phys. Rev. D **98**, 102006 (2018). https://doi.org/10.1103/PhysRevD.98.102006
3. C.E. Aalseth et al., Eur. Phys. J. Plus **133**(3), 131 (2018). https://doi.org/10.1140/epjp/i2018-11973-4
4. A. Badertscher et al., J. Instrum. **8**(09), C09005 (2013). https://doi.org/10.1088/1748-0221/8/09/C09005
5. K. Rielage et al., Phys. Proc. **61**, 144 (2015). https://doi.org/10.1016/j.phpro.2014.12.024. (**13th International Conference on Topics in Astroparticle and Underground Physics, TAUP 2013**)
6. M. Boulay, A. Hime, Astropart. Phys. **25**(3), 179 (2006). https://doi.org/10.1016/j.astropartphys.2005.12.009
7. P. Adhikari et al., Eur. Phys. J. C (2020). https://doi.org/10.1140/epjc/s10052-020-7789-x
8. P. Adhikari et al., Eur. Phys. J. C (2021). https://doi.org/10.1140/epjc/s10052-021-09514-w
9. D. Gastler et al., Phys. Rev. C **85**, 065811 (2012). https://doi.org/10.1103/PhysRevC.85.065811
10. C. Regenfus, Y. Allkofer, C. Amsler, W. Creus, A. Ferella, J. Rochet, M. Walter, J. Phys. Conf. Ser. **375**(1), 012019 (2012). https://doi.org/10.1088/1742-6596/375/1/012019
11. H. Cao et al., Phys. Rev. D **91**, 092007 (2015). https://doi.org/10.1103/PhysRevD.91.092007
12. P. Agnes et al., Phys. Rev. D **97**, 112005 (2018). https://doi.org/10.1103/PhysRevD.97.112005
13. J. Lindhard, V. Nielsen, M. Scharff, P.V. Thomsen, Kgl. Danske Videnskab., Selskab. Mat. Fys. Medd. **33**(10) (1963). https://www.osti.gov/biblio/4701226
14. D.M. Mei, Z.B. Yin, L. Stonehill, A. Hime, Astropart. Phys. **30**(1), 12 (2008). https://doi.org/10.1016/j.astropartphys.2008.06.001
15. A. Hitachi, Instruments **5**(1) (2021). https://doi.org/10.3390/instruments5010005. https://www.mdpi.com/2410-390X/5/1/5
16. T. Doke, H.J. Crawford, A. Hitachi, J. Kikuchi, P.J. Lindstrom, K. Masuda, E. Shibamura, T. Takahashi, Nucl. Instrum. Methods Phys. Res. Sect. A Acceler. Spectrom. Detect. Assoc. Equip. **269**(1), 291 (1988). https://doi.org/10.1016/0168-9002(88)90892-3
17. A. Hitachi, T. Takahashi, T. Hamada, E. Shibamura, N. Funayama, K. Masuda, J. Kikuchi, T. Doke, Nucl. Instrum. Methods Phys. Res. **196**(1), 97 (1982). https://doi.org/10.1016/0029-554X(82)90622-X
18. J.A. LaVerne, A. Hitachi, J.J. Kolata, T. Doke, Phys. Rev. B **54**, 15724 (1996). https://doi.org/10.1103/PhysRevB.54.15724
19. B. Singh, M.S. Basunia, M. Martin et al., Nucl. Data Sheets **160**, 405 (2019)
20. S. Zhu, E.A. Mccutchan, Nucl. Data Sheets **175**, 1 (2021)
21. M.S. Basunia, Nucl. Data Sheets **121**, 561 (2014)

22. S. Chu, L. Ekström, R. Firestone, The Lund/LBNL Nuclear Data Search, Version 2.0 (1999). http://nucleardata.nuclear.lu.se/toi/
23. P.A. Amaudruz et al., Astropart. Phys. **108**, 1 (2019). https://doi.org/10.1016/j.astropartphys.2018.09.006
24. P.A. Amaudruz et al., Nucl. Instrum. Methods Phys. Res. Sect. A Acceler. Spectrom. Detect. Assoc. Equip. **922**, 373 (2019). https://doi.org/10.1016/j.nima.2018.12.058
25. T. Bolton et al., RAT (is an Analysis Tool) User's Guide (2018). https://rat.readthedocs.io/en/latest/
26. M. Hatlo, F. James, P. Mato, L. Moneta, M. Winkler, A. Zsenei, IEEE Trans. Nucl. Sci. **52**(6) (2005)
27. R. Brun, F. Rademakers, Nucl. Instrum. Methods Phys. Res. Sect. A Acceler. Spectrom. Detect. Assoc. Equip. **389**(1), 81 (1997). https://doi.org/10.1016/S0168-9002(97)00048-X. (**New Computing Techniques in Physics Research V**)
28. J.B. McLaughlin, Corrections to signal saturation on the DEAP-3600 dark matter search. Master's thesis, Queen's University Kingston, Ontario (2018)
29. E. Aprile, K.L. Giboni, P. Majewski, K. Ni, M. Yamashita, R. Hasty, A. Manzur, D.N. McKinsey, Phys. Rev. D **72**, 072006 (2005). https://doi.org/10.1103/PhysRevD.72.072006
30. F. Arneodo et al., Nucl. Instrum. Methods Phys. Res. Sect. A Acceler. Spectrom. Detect. Assoc. Equip. **449**(1), 147 (2000). https://doi.org/10.1016/S0168-9002(99)01300-5
31. D. Akimov et al., Phys. Lett. B **524**(3), 245 (2002). https://doi.org/10.1016/S0370-2693(01)01411-3
32. R. Brunetti et al., New Astron. Rev. **49**(2), 265 (2005). https://doi.org/10.1016/j.newar.2005.01.017. (**Sources and Detection of Dark Matter and Dark Energy in the Universe**)
33. J.F. Ziegler, J.P. Biersack, M.D. Ziegler. SRIM software. http://www.srim.org/
34. J.F. Ziegler, J.P. Biersack, *The Stopping and Range of Ions in Matter* (Springer US, Boston, 1985), pp. 93–129. https://doi.org/10.1007/978-1-4615-8103-1_3
35. J.B. Birks, Proc. Phys. Soc. Sect. A **64**(10), 874 (1951). https://doi.org/10.1088/0370-1298/64/10/303